Article

Modification of the Microstructure and Transport Properties of La$_2$CuO$_{4−\delta}$ Electrodes via Halogenation Routes

Lucía dos Santos-Gómez [1,*], Javier Zamudio-García [2], José M. Porras-Vázquez [2], Enrique R. Losilla [2] and David Marrero-López [3]

1   Department of Physical and Analytical Chemistry, University of Oviedo—CINN-CSIC, 33006 Oviedo, Spain
2   Departamento de Química Inorgánica, Cristalografía y Mineralogía, Universidad de Málaga, 29071 Málaga, Spain; zamudio@uma.es (J.Z.-G.); josema@uma.es (J.M.P.-V.); r_losilla@uma.es (E.R.L.)
3   Departamento de Física Aplicada I, Universidad de Málaga, 29071 Málaga, Spain; marrero@uma.es
*   Correspondence: ldsg@uniovi.es; Tel.: +34-9851-029-65

Abstract: Ruddlesden–Popper type electrodes with composition La$_2$CuO$_{4−\delta}$ are alternative cathode materials for solid oxide fuel cells (SOFCs); however, the undoped compound exhibits low electrical conductivity for potential applications, which is usually increased by alkaline-earth doping. A promising alternative to alkaline-earth doping is the modification of the anionic framework by halogen doping. In this study, La$_2$CuO$_{4−0.5x}$A$_x$ (A = F, Cl, Br; x = 0–0.3) compounds are prepared by a freeze-drying precursor method, using an anion doping strategy. The composition, structure, morphology and electrical properties are studied to evaluate their potential use in solid oxide fuel cells (SOFCs). The halogen-doped materials show higher electrical conductivity and improved electrocatalytic activity for oxygen reduction reactions when compared to the pristine material, with polarization resistance values 2.5 times lower, i.e., 0.20, 0.11 and 0.08 Ω cm^2 for undoped, F- and Cl-doped samples, respectively, at 800 °C. Moreover, halogen doping prevents superficial copper segregation in La$_2$CuO$_{4−\delta}$, making it an attractive strategy for the development of highly efficient electrodes for SOFCs.

Keywords: La$_2$CuO$_{4−\delta}$; Ruddlesden–Popper; anion doping; halogenation; solid oxide fuel cell

1. Introduction

There is great interest in developing intermediate-temperature solid oxide fuel cells (IT-SOFCs) to overcome the drawbacks related to durability and manufacturing costs that still hinder the wide commercialization of these electrochemical devices [1–5]. Nevertheless, decreasing the operating temperature involves a considerable reduction in the activity of the electrodes, especially for the cathode material.

The main function of the cathode is to provide active sites for the oxygen reduction reactions (ORRs); thus, high ionic and electronic conductivity values are needed [6]. Nowadays, the most employed cathode material for SOFC application is La$_{1−x}$Sr$_x$MnO$_{3−\delta}$ (LSM), which has a high electronic conductivity value (235 S cm$^{−1}$ at 900 °C) and is compatible with most common electrolyte materials, Zr$_{0.84}$Y$_{0.16}$O$_{1.92}$ (YSZ) [7]. However, the poor ionic transport properties of LSM restricts its use at temperatures below 800 °C [8]. Other cathode materials with perovskite-type structures are the La$_{1−x}$Sr$_x$Co$_{1−y}$Fe$_y$O$_{3−\delta}$ (LSCF) (x ≤ 0.6; 0 ≤ y ≤1) series, which present higher mixed ionic and electronic conductivity when compared to LSM, although these materials are not compatible with YSZ [9,10]. Another drawback of Sr-containing perovskite cathodes is the tendency of Sr to segregate on the electrode surface, blocking the active sites for the ORR and decreasing the electrode efficiency [11]. Hence, the development of durable cathodes without alkaline-earth elements is still a major concern for the viability of this technology [12].

Ruddlesden–Popper-type electrodes, *Ln*$_2$MO$_{4−\delta}$ (*Ln* = La, Pr and Nd; M = Ni and Cu), are promising cathode materials with improved oxygen transport properties [13,14].

Moreover, the lack of alkaline-earth elements makes them less prone to surface phase segregation [15–17]. Among these Ruddlesden–Popper-type phases, lanthanum nickelates ($La_2NiO_{4-\delta}$) have received great attention due to their high electronic conductivity [15,17–19]. However, sintering temperatures above 1200 °C are needed to obtain a single compound [20]. In contrast, lanthanum cuprates ($La_2CuO_{4-\delta}$) [21] can be synthesized as pure compounds at only 800 °C, much lower than that of the analogous nickelates, although their electrical conductivity is substantially lower [22–25].

Lanthanum cuprates have been intensively studied in the literature due to their superconducting properties at low temperature [26]; however, some studies have also reported their potential use as SOFC cathodes [24,27,28]. $La_2CuO_{4-\delta}$ is a mixed ionic and electronic conductor due to the presence of intrinsic oxygen vacancies in the structure. In order to further improve the conductivity, La^{3+} is partially replaced by Sr^{2+}, generating additional oxygen vacancies in the lattice. Thus, the tailoring of the oxygen non-stoichiometry has a significant impact on the structure and electrochemical properties of these materials. For instance, Kanai et al. reported the ability of $La_{2-x}Sr_xCuO_{4-\delta}$ to create different types of oxygen defects, i.e., oxygen vacancies and interstitial oxygens, by varying the oxygen partial pressure, Sr content and synthesis temperature [29]. Mazo et al. reported that $La_{2-x}Sr_xCuO_{4-\delta}$ presented high oxygen diffusivity in the temperature range of 475–725 °C, with $La_{1.63}Sr_{0.37}CuO_{4-\delta}$ being the composition with the highest value of ~10^{-6} cm^2 s^{-1} [30].

A promising alternative to alkaline-earth doping is the modification of the anionic framework by halogen doping, which weakens the metal–oxygen bond energy and favors oxygen mobility during the ORR [31]. Recently, the electrochemical performance of single and layered perovskite-type electrodes, such as $SrFe_{0.9}Ti_{0.9}O_{3-\delta}$, $Sr_2Fe_{1.5}Mo_{0.5}O_{6-\delta}$, $La_{0.5}Ba_{0.5}FeO_{3-\delta}$ and $NdBaCoFeO_{5+\delta}$, have been enhanced by anion doping, improving the oxygen surface exchange coefficients and decreasing the polarization resistance [32–35]. For instance, Zhang et al. observed a change in the crystal symmetry of $Sr_2Fe_{1.5}Mo_{0.5}O_{6-x-\delta}F_x$, SFMF, x = 0, 0.1, 0.2 and 0.3), as well as enhanced electrocatalytic activity for the ORR with a polarization resistance of 0.072 Ω cm^2 at 800 °C [31].

F doping has also been proved successful in enhancing the electrical properties of triple-conducting materials (H^+, O^{2-} and e^-), such as $BaCo_{0.4}Fe_{0.4}Zr_{0.1}Y_{0.1}O_{3-\delta}$ and $Pr_2NiO_{4-\delta}$, improving both the oxygen exchange capability and hydration of the electrodes [36,37]. Some authors have successfully introduced F^- and Cl^- into the $La_2CuO_{4-\delta}$ structure, and the resulting materials achieved different superconducting properties [38,39]. For example, Adachi et al. investigated superconductivity in $La_2CuO_{4-x}F_x$ samples, which were synthesized by heating $La_2CuO_{4-\delta}$ with NH_4F as a fluorinating reagent at 240 °C under O_2 flow [38].

The aim of this work is to synthesize new alkaline-earth-free cathode materials based on $La_2CuO_{4-\delta}$ by employing an anion doping strategy with different halogen elements to improve their electrochemical properties for ORRs. $La_2CuO_{4-0.5x}A_x$ (A = F, Cl, Br; x = 0–0.3) compounds are prepared by using a freeze-drying precursor method. This is a dehydration process at low temperature widely used in the pharmaceutical and food industry, which has proved to be a versatile route for obtaining stoichiometrically controlled precursors. This is a simple and economic procedure to obtain large amounts of powders without a rigorous control of the cation concentration, chelating agent and temperature during the water evaporation, compared to other alternative routes, such as sol–gel or combustion [40,41]. The structure, composition, morphology and electrochemical properties of these electrodes are studied by using different techniques to evaluate their potential use in SOFCs.

2. Materials and Methods

2.1. Synthesis of Materials

$La_2CuO_{4-\delta}$ polycrystalline powders were synthesized using a freeze-drying precursor method, following the procedure described previously [42]. Briefly, aqueous cation solutions were prepared separately by dissolving stoichiometric amounts of La_2O_3 (99.9%, Sigma-Aldrich, St. Louis, MO, USA) in diluted nitric acid and $Cu(NO_3)_2 \cdot 3H_2O$ (99.5%,

Sigma-Aldrich) in distilled water. Both solutions were mixed with ethylenediaminete-traacetic acid (99.9%, Sigma-Aldrich) in a ligand:metal molar ratio = 1:1. This solution was frozen in liquid N_2 and freeze-dried for 48 h [42]. The dried precursors were calcined at 800 °C for 2 h to obtain the polycrystalline compound.

The intercalation of the halogens F, Cl and Br was carried out by mixing, in an agate mortar, stoichiometric amounts of $La_2CuO_{4-\delta}$ with the different halogenating reagents for 15 min: polytetrafluoroethylene (PTFE) (99.9%, Sigma-Aldrich), polyvinyl chloride (PVC) (99.9%, Sigma-Aldrich) and 4-Bromophenyl ether (99%, Sigma-Aldrich). After that, the mixtures were heated at 360 °C for 12 h with a heating and cooling rate of 1 and 5 °C min^{-1}, respectively. Finally, the powders were pressed into disks of 13 and 1 mm of diameter and thickness, respectively, and heated between 1000 and 1100 °C for 1 h. Hereafter, the $La_2CuO_{4-0.5x}A_x$ (A = F, Cl, Br; x = 0–0.3) series will be denoted as A_x, where A and x indicate the type and content of the halogen element employed, respectively, and the pristine sample ($La_2CuO_{4-\delta}$) will be labeled as LCO.

2.2. Structural, Morphological and Electrochemical Characterization

The structure and composition of the samples were analyzed with X-ray powder diffraction (XRPD) by using a PANalytical X'Pert PRO diffractometer with monochromatic $CuK_{\alpha,1}$ radiation. GSAS and X'Pert HighScore Plus software were employed to carry out the structural analysis and the phase identification, respectively [43,44].

The morphology was studied with field emission scanning electron microscopy (FE-SEM) by using an FEI Helios Nanolab 650 and energy-dispersive X-ray spectrometer (EDS, X-Max, Oxford Instruments, Oxford, UK).

The conductivity was determined by using the four-probe Van der Pauw method. Four platinum small contacts and wires were attached symmetrically on the pellet surface for the electrical connections. The conductivity was determined from the average values of two different pellets. The measurements were conducted in static air between room temperature and 800 °C.

The electrode polarization resistance (R_p) was determined using impedance spectroscopy (Solartron 1260 FRA) in symmetrical cells and two electrode configurations. The spectra were collected at frequencies ranging from 0.01 to 10^6 Hz in air and as a function of the oxygen partial pressure by using an electrochemical cell equipped with an oxygen pump and sensor [45,46]. The AC amplitude was set to 25 mV between 400 and 800 °C to study the electrode polarization response and set to 100 mV below that temperature range to study the electrolyte response and possible chemical reactions at the electrode/electrolyte interface. Dense pellets of $Ce_{0.9}Gd_{0.1}O_{1.95}$ (CGO) electrolyte were prepared by pressing the commercial powders (Rhodia) into pellets of 10 and 1 mm of diameter and thickness, respectively, and then sintered at 1400 °C for 4 h. The A_x powders were mixed with De-coflux™ binder (Zschimmer & Schwarz, Lahnstein, Germany) until a homogeneous slurry was obtained. Symmetrical cells were constructed by painting the ink onto CGO pellets and then sintering them at 800 °C for 1 h to ensure adequate adherence to the electrolyte. Different current collectors made of Pt, Au and Pt paste (Metalor, Marin, Switzerland) were used and reproducible results were obtained, which suggested the negligible influence of the current collector on the electrode polarization response. The overall polarization resistance was determined from the interception of the impedance spectra at high and low frequency with the Z'-axis. Furthermore, the data were analyzed by the distribution of relaxation times to identify the different electrochemical processes involved in the ORR [47].

3. Results

3.1. Structural Properties of $La_2CuO_{4-0.5x}A_x$ (A = F, Cl, Br; x = 0–0.3) Series

Figure 1 shows the evolution of the XRPD patterns of undoped LCO with increasing sintering temperature. The main phase formed at 600 °C corresponds to LCO, but some additional peaks assigned to the secondary phases, such as CuO, La_2O_3 and $La_2O_2(CO_3)$, are also observed due to the incomplete reaction of the precursors at this low temperature.

LCO becomes a single phase after heating at 800 °C, and no evidence of additional phases is detected up to 1000 °C.
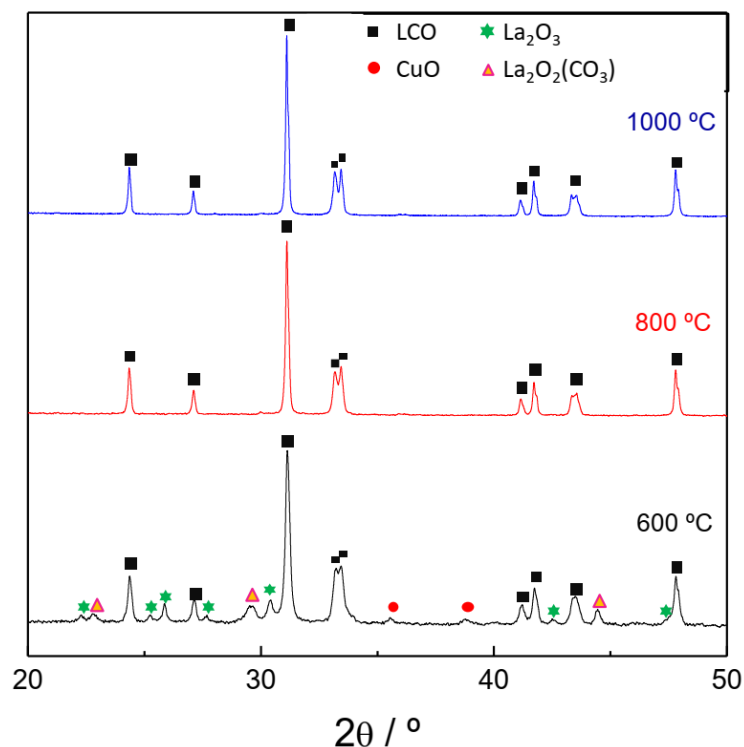

Figure 1. XRPD patterns of $La_2CuO_{4-\delta}$ sintered at 600, 800 and 1000 °C for 1 h.

Figure 2 displays the XRPD patterns of the $La_2CuO_{4-0.5x}A_x$ (A = F, Cl, Br; x = 0.1–0.3) series sintered at 1000 and 1100 °C for 1 h. All compounds crystallize with orthorhombic symmetry. In the F-doped series, it is observed that $F_{0.1}$ is in a single phase at 1000 °C (Figure 2a). However, extra diffraction peaks assigned to LaOF (PDF number: 00-006-0281) are observed when the fluorine content increases above x = 0.1. In this case, it is necessary to increase the temperature to 1100 °C to completely incorporate the F^- into the $La_2CuO_{4-\delta}$ structure. LaOF is also detected for the $F_{0.3}$ sample sintered at 1100 °C, suggesting that the solubility limit of F^- in $La_2CuO_{4-\delta}$, under the experimental conditions used in this work, is close to x = 0.2.

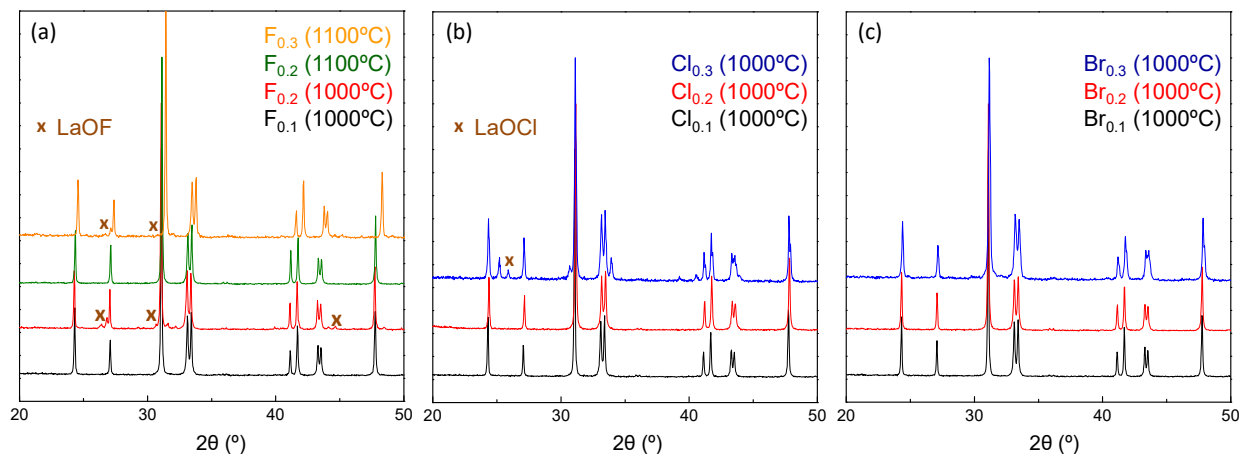**Figure 2.** XRPD patterns of (**a**) $La_2CuO_{4-0.5x}F_x$ (x = 0–0.3), (**b**) $La_2CuO_{4-0.5x}Cl_x$ (x = 0–0.3) and (**c**) $La_2CuO_{4-0.5x}Br_x$ (x = 0–0.3), sintered at 1000 and 1100 °C for 1 h.

The $Cl_{0.1}$ and $Cl_{0.2}$ compositions are pure compounds at 1000 °C without the presence of extra diffraction peaks; however, a secondary phase of LaOCl (PDF number: 00-008-0477) is detected in samples with a higher Cl content (Figure 2b). Thus, the solubility limit of Cl^- into the $La_2CuO_{4-\delta}$ structure is also close to x = 0.2. In the case of Br-containing samples, diffraction peaks ascribed to the secondary phases are not detected at 1000 °C for the compositions until x = 0.3, which may be related to the high volatility of Br at sintering temperatures, and also the formation of non-stable secondary phases (Figure 2c).

A detailed inspection of the XRPD patterns reveals that the halogen intercalation produces a slight shift in the diffraction peaks to lower angles due to an increase in the lattice cell volume. These results are in accordance with those previously reported in the literature for F- and Cl-doped $La_2CuO_{4-\delta}$ [38,39]. In general, it is expected that the lattice expansion could facilitate oxygen ion migration and improve the ORR catalytic activity [38].

The XRPD data were analyzed using the Rietveld method by using the different structural models reported previously in the Inorganic Crystal Structure Database (ICSD) [27,48]. Figure 3 shows the XRPD Rietveld plots of LCO, $F_{0.2}$, $Cl_{0.2}$ and $Br_{0.2}$ as representative examples of the series. The best fits for all compositions are achieved with orthorhombic symmetry (*Fmmm*, space group), with good agreement factors (Table 1). The typical parameters were refined, including scale factor, background, peak shape and lattice constant. The atomic occupations were fixed to the stoichiometry of each sample. The evolution of the unit cell parameters with their halogen content is summarized in Table 1. The cell volume for F-doped samples slightly increases upon F doping from 380.64 Å^3 for x = 0 to 380.76 Å^3 for x = 0.2, despite the ionic radii of F^- (1.33 Å) being slightly lower than that of O^{2-} (1.4 Å). This may be explained by the change in the oxidation state of copper, as well as variation in the oxygen concentration vacancies in the structure to compensate for the deficiency in terms of the negative electrical charge. In the case of the Cl_x series, the unit cell volume also increases upon Cl doping, varying from 380.64 Å^3 for LCO to 381.46 Å^3 for $Cl_{0.2}$. The $Cl_{0.3}$ sample does not follow the same trend due to the presence of LaOCl as a secondary phase. Finally, the Br-doped samples exhibit a small increase in the unit cell with increasing Br content, which is in agreement with the higher ionic radii of Br^- (1.96 Å) compared to O^{2-} (1.4 Å) (Table 1). This seems to indicate that a certain amount of bromine is incorporated inside the $La_2CuO_{4-\delta}$ structure after sintering at 1000 °C. The evolution of the conductivity with halogen doping will provide further evidence on the incorporation of these elements in $La_2CuO_{4-\delta}$.

Table 1. Cell parameters, cell volumes and disagreement factors for $La_2CuO_{4-0.5x}A_x$ (A = F, Cl and Br; x = 0–0.3) samples obtained from XRPD data analysis.

	a (Å)	b (Å)	c (Å)	V (Å^3)	R_{WP} (%)	R_F (%)
LCO (1000 °C)	5.3563 (1)	5.4026 (1)	13.1543 (3)	380.64 (2)	7.78	1.74
$F_{0.1}$ (1000 °C)	5.3562 (1)	5.4038 (1)	13.1517 (3)	380.68 (2)	7.32	1.42
$F_{0.2}$ (1100 °C)	5.3571 (1)	5.4049 (1)	13.1515 (3)	380.76 (2)	8.14	2.36
$Cl_{0.1}$ (1000 °C)	5.3567 (1)	5.4038 (1)	13.1523 (3)	380.72 (2)	7.45	1.32
$Cl_{0.2}$ (1000 °C)	5.3605 (2)	5.4078 (2)	13.1589 (4)	381.46 (3)	7.45	2.38
$Cl_{0.3}$ (1000 °C)	5.3538 (4)	5.3997 (4)	13.144 (1)	380.00 (7)	12.65	3.62
$Br_{0.1}$ (1000 °C)	5.3567 (1)	5.4044 (1)	13.1510 (3)	380.72 (2)	7.91	1.65
$Br_{0.2}$ (1000 °C)	5.3569 (1)	5.4050 (1)	13.1511 (3)	380.76 (2)	7.51	1.84
$Br_{0.3}$ (1000 °C)	5.3572 (2)	5.4052 (2)	13.1514 (7)	380.82 (5)	7.86	1.84
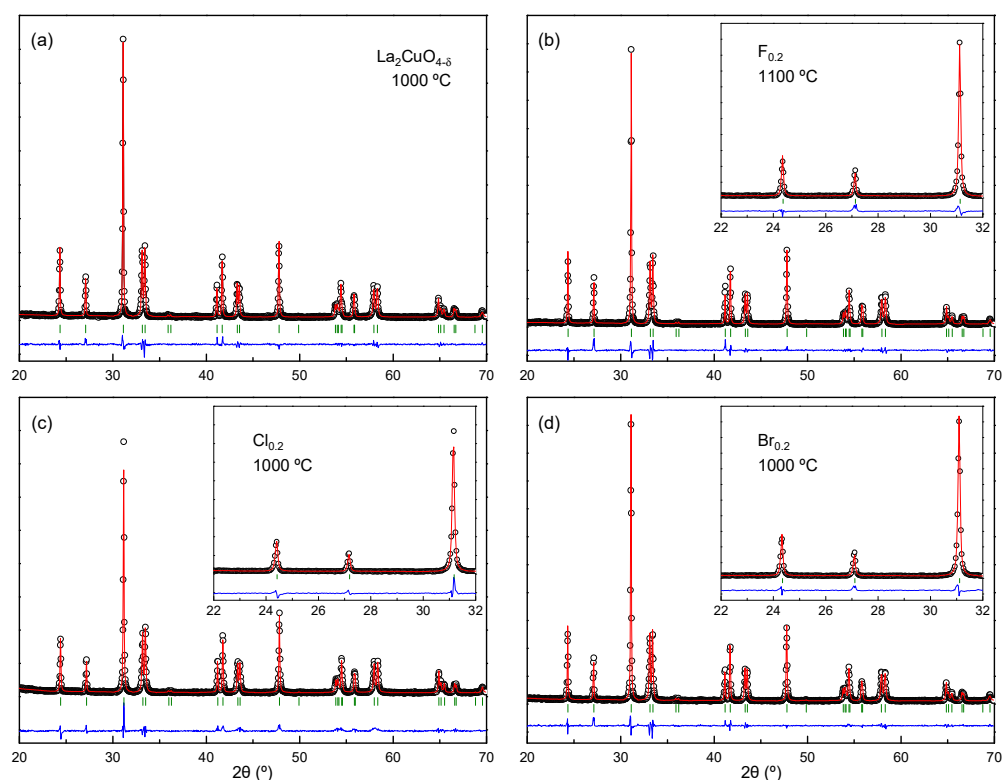
Figure 3. Rietveld refinement plots of (**a**) La$_2$CuO$_{4-\delta}$, (**b**) F$_{0.2}$, (**c**) Cl$_{0\cdot 2}$ and (**d**) Br$_{0.2}$ sintered at 1000 or 1100 °C for 1 h.

3.2. Microstructural Analysis

SEM images of LCO pellets, sintered at 1000 °C for 1 h, are shown in Figure 4. The pellets are fully dense with an average particle size of approximately 4 μm; however, small grains of ~0.5 μm diameter, ascribed to phase segregation, are observed at the grain boundary region of the pellet surface. Phase segregations were analyzed using EDS and assigned to a Cu-rich phase. It has to be noted that this phase segregation was only detected with SEM-EDS analysis but not with XRPD (Figure 4b–d). In previous studies, La$_2$CuO$_{4-\delta}$ calcined above 1050 °C showed some additional diffraction peaks in the pattern, attributed to the partial decomposition of the compound into CuO, Cu$_2$O and Cu [49].

To further study the origin of this phase segregation, LCO pellets were sintered at 800, 900 and 1000 °C for 1 h. The cross-sectional SEM images and the EDS analysis of these pellets are shown in Figure 4e,f. As it is expected, the grain size and the densification of the samples increase along with the sintering temperature. The average grain size grows from 0.25 μm at 800 °C to 4 μm at 1000 °C, while the relative density increases from 70 to 95% in the same temperature range. A homogeneous distribution of the elements is observed in the cross-sectional image of the pellets without any evidence of copper segregation. This suggests that copper segregation is a superficial phenomenon due to the high diffusion rate of copper and its easy migration towards the surface. Thus, the sintering temperature of these materials needs to be as low as possible to avoid this drawback.

Figure 5 shows some representative EDS analysis of the surface and cross-section of the pellets for F$_{0.2}$, Cl$_{0.2}$ and Br$_{0.2}$ samples sintered at different temperatures. The EDS analysis confirms the presence of halogen elements in all the samples which is in good agreement with the XRPD results. More interestingly, no superficial segregation is detected for F$_{0.2}$ sintered at 1100 °C (Figure 5a) and Cl$_{0.2}$ sintered at 1000 °C (Figure 5c), indicating that halogen doping prevents superficial copper segregation at high sintering temperatures.
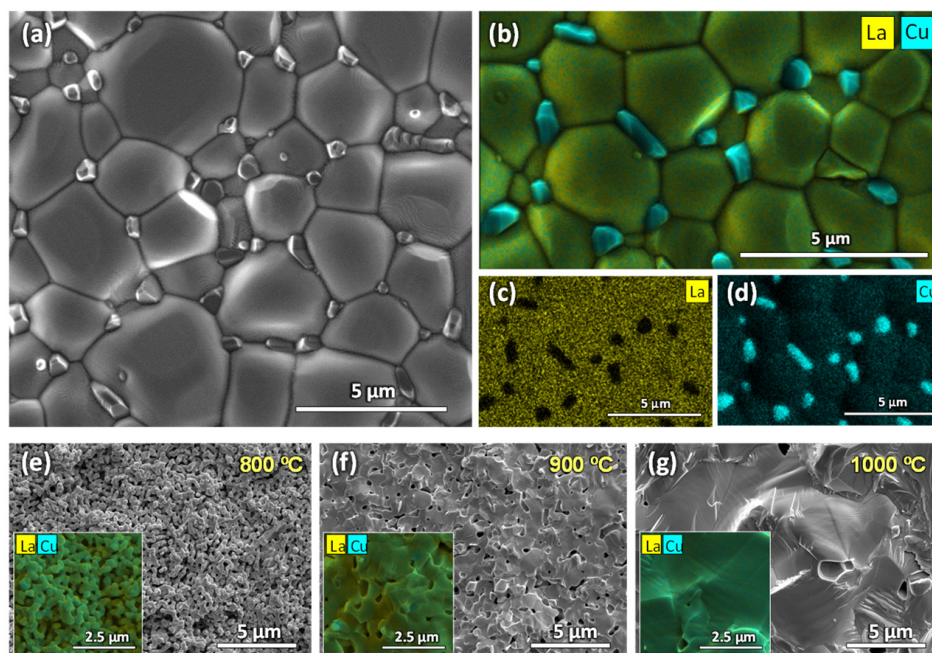
Figure 4. (**a**) Surface SEM image and the corresponding (**b**–**d**) EDS of LCO sintered at 1000 °C for 1 h. Cross-sectional SEM images and EDS of $La_2CuO_{4-\delta}$ pellets sintered at (**e**) 800, (**f**) 900 and (**g**) 1000 °C for 1 h.
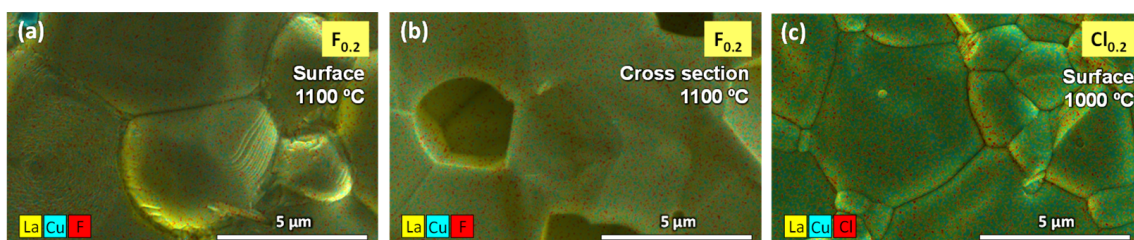

Figure 5. SEM-EDS analysis of (**a**) surface and (**b**) cross-section of $F_{0.2}$ sintered at 1100 °C for 1 h. SEM-EDS analysis of the surface of (**c**) $Cl_{0.2}$ sintered at 1000 for 1 h.

3.3. Electrochemical Properties

3.3.1. Conductivity

The conductivity of the $La_2CuO_{4-0.5x}A_x$ (A = F, Cl, Br; x = 0.1, 0.2) series is investigated as a function of the temperature (Figure 6). In general, the conductivity of all samples is little affected by the temperature, similarly to previous works for undoped and cation-doped $La_2CuO_{4\pm\delta}$ cathodes [22,50]. Metallic-like behavior is observed for all the samples in the whole temperature range studied (150–800 °C); however, F-doped samples experience a more pronounced decrease in conductivity between 100 and 400 °C, which requires further studies to fully explain this observation. The pristine LCO exhibits conductivity values of about 5 S cm^{-1}, while the incorporation of the halogen elements produces a significant increase in the total conductivity. For instance, the conductivity of Cl-doped samples at 800 °C increases to 11 and 15 S cm^{-1} for $Cl_{0.1}$ and $Cl_{0.2}$, respectively. The introduction of Br in the structure also produces an enhancement in the conductivity of ~20 S cm^{-1} for $Br_{0.2}$ at 800 °C. The highest conductivity values are found for F-doped samples, e.g., 15 and 35 S cm^{-1} for $F_{0.1}$ and $F_{0.2}$, respectively, at 800 °C. By considering that the electrical conductivity in $La_2CuO_{4\pm\delta}$ is attributed to a small polaron hopping mechanism, the conductivity improvement after halogen doping is mainly associated with a change in the fraction of Cu^{2+}/Cu^+ species to compensate for the deficiency of a negative electrical charge, similarly to Sr doping in $La_2CuO_{4\pm\delta}$ [22]. These results further confirm that these halogens are incorporated in the LCO lattice and modify the electrical properties.

Moreover, the conductivity increases, following the trend Br < Cl < F for the same halogen content, which is possibly explained by the lower lattice distortion produced by F (1.33 Å) in comparison to Cl (1.8 Å) and Br (1.96 Å) which have higher ionic radii [51].
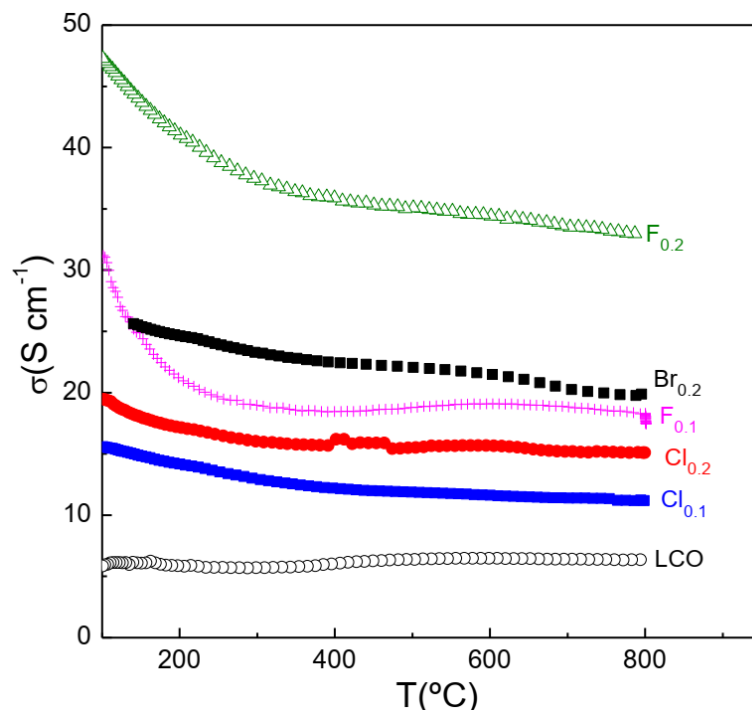

Figure 6. Variation of the conductivity with the temperature for $La_2CuO_{4-0.5x}A_x$ (A = F, Cl, Br; x = 0.1, 0.2) series and undoped electrode (LCO).

3.3.2. Electrode Polarization Resistance

The electrochemical properties of these materials for the ORR were investigated using impedance spectroscopy in symmetric cell configurations with $Ce_{0.9}Gd_{0.1}O_{1.95}$ (CGO) electrolytes. The chemical compatibility between LCO and CGO was previously studied, demonstrating good chemical stability at temperatures below 900 °C [27]. A cross-sectional image of the LCO/CGO/LCO symmetrical cells sintered at 800 °C is shown in Figure 7. The electrode, with a thickness of 35 ± 5 µm estimated from different SEM images, shows good adherence to the electrolyte without cracks or delamination after the electrochemical test. In addition, it has high porosity to facilitate the oxygen transport to the electrochemical active sites for the electrochemical reactions.
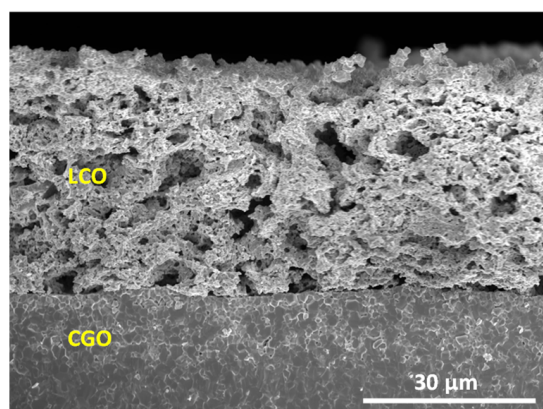

Figure 7. Cross-sectional SEM image of the LCO-CGO symmetrical cells sintered at 800 °C for 1 h.

The representative impedance spectra for the pristine and halogenated samples are represented in Figure 8a. Notice that the serial resistance was substrate for the better comparison of the electrode response. Nevertheless, the serial resistance of the cells is similar to the blank CGO electrolyte with only Pt electrodes. In addition, additional contributions to the CGO electrolyte, i.e., bulk and grain boundary, are not observed at low temperatures, indicating a negligible chemical reaction at the electrode/electrolyte interface (Figure S1, Supplementary Information).
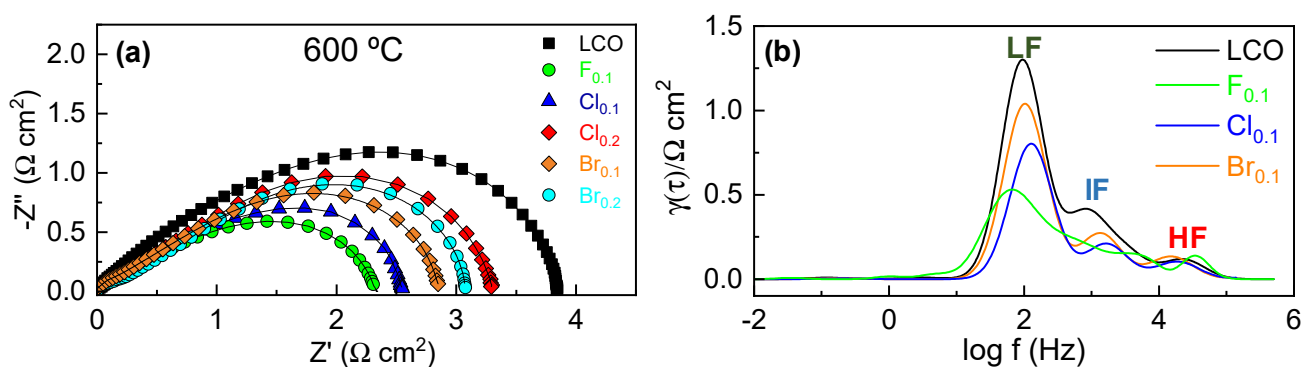

Figure 8. (**a**) Impedance spectra at 600 °C and the corresponding (**b**) distribution of relaxation times curves of $La_2CuO_{4-0.5x}A_x$ (A = F, Cl, Br; x = 0, 0.1) series.

As can be observed, a substantial decrease in the polarization resistance (R_p) is observed for the halogenated samples. Such an improvement in the ORR activity is explained by the incorporation of the halogens into the LCO structure, which improves the mobility of the oxygen vacancies in the lattice and increases both the ionic and electronic conductivity [33]. Halogen doping above x > 0.1 leads to higher R_p values, which are possibly associated with secondary phase segregation, as previously observed using XRPD. Notice also that the electrochemical measurements of $F_{0.2}$ were not performed due to the higher sintering temperature necessary to achieve a single-phase compound.

The impedance spectra were analyzed using the distribution of relaxation times (DRT) to distinguish the different electrochemical processes (Figure 8b) [52–54]. The undoped and halogen-doped electrodes show three peaks at practically the same frequency, suggesting that the same electrochemical processes are involved in the ORR. However, a slight shift in the relaxation frequencies is observed at lower frequencies, especially for $F_{0.1}$, a fact that could be linked to better oxide ion transport or extended active sites for ORRs [55].

To obtain further information on the electrochemical processes, the impedance spectra of $F_{0.1}$ were collected at different oxygen partial pressures (pO_2) (Figure 9a), and the corresponding DRT curves are given in Figure 9b. Three different contributions are clearly observed in the pO_2 range studied. These resistances depend on the oxygen partial pressure according to the relation $R = R_o(pO_2)^{-m}$, where the reaction order m provides information on the electrochemical process involved in the ORR (Figure 9c) [45,46]. The main contribution to the total polarization resistance at low frequency (LF) with m∼0.25 is unequivocally assigned to a charge transfer process on the electrode surface [56,57]. The high (HF) and intermediate (IF) processes are independent of pO_2 with a reaction order m∼0, which are attributed to oxide ion transport at the electrode/electrolyte interface and to current losses between the current collector and the electrode, respectively [58]. Diffusion limitation processes at very low frequency with $m = 1$ are not observed.
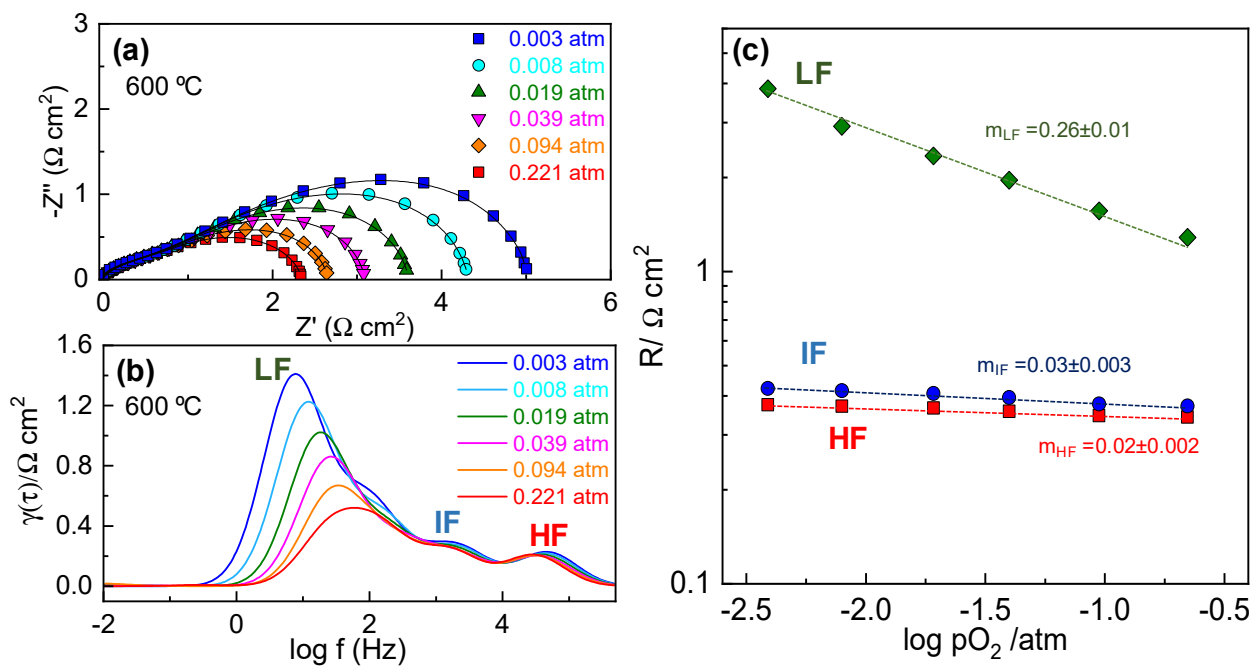
Figure 9. (**a**) Impedance spectra as function of the pO_2 at 600 °C and the corresponding (**b**) distribution of relaxation times analysis of $F_{0.1}$ sample. (**c**) Variation in the polarization resistance of the different electrode contributions on pO_2.

Figure 10 shows the variation of Rp with the temperature for LCO, $F_{0.1}$, $Cl_{0.1}$, $Cl_{0.2}$, $Br_{0.1}$ and $Br_{0.2}$. It is evident that Rp values for halogenated samples are lower than those for the pristine LCO and this variation is more accused in the high temperature range. For instance, Rp values for the LCO, $F_{0.1}$ and $Cl_{0.1}$ are 3.8, 2.29 and 2.54 Ω cm^2, respectively, at 600 °C. Moreover, the lowest Rp values are achieved for halogenated samples with x = 0.1 and increases above this content. These values of Rp are significantly lower than those obtained for a blank CGO electrolyte with only Pt electrodes ~50 Ωcm^2, indicating a negligible influence of the Pt current collector on the electrode performance [59].

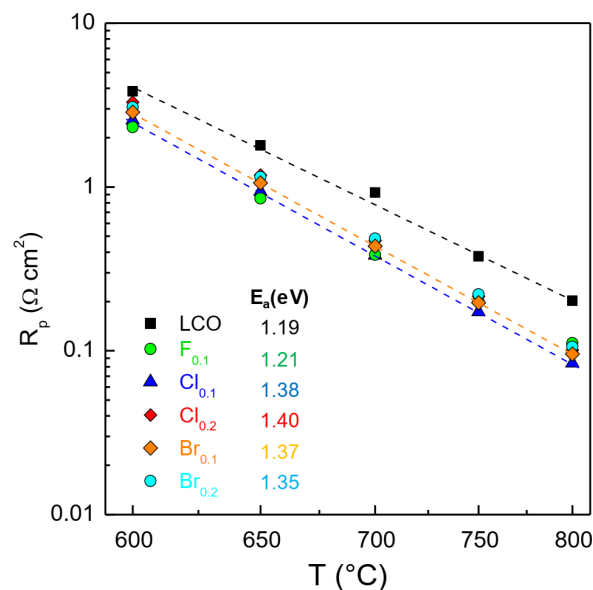**Figure 10.** Variation of the total polarization resistance with the temperature of $La_2CuO_{4-0.5x}A_x$ (A = F, Cl, Br; x = 0–0.2) series.

The values of activation energy seem to increase upon doping, especially for high doping levels between 1.19 eV for LCO and 1.40 eV for $Cl_{0.2}$ (inset of Figure 10). Such behavior may be related to excessive oxygen lattice distortion. In this context, previous studies have demonstrated that an optimum level of F doping enhances the crystal symmetry and facilitates the migration of oxide ions [31]. Thus, these results indicate that only a small quantity of the halogenated element is required for improving the electrochemical activity of $La_2CuO_{4-\delta}$-based electrodes, thus avoiding the use of alkaline-earth doping, such as Sr^{2+} and Ba^{2+}, which are prone to segregate on the electrode surface [11].

4. Conclusions

A series of novel cathode materials with Ruddlesden–Popper-type structures, which are alkaline-earth-free, was investigated. The $La_2CuO_{4-0.5x}A_x$ (A = F, Cl, Br; x = 0–0.3) compounds were prepared by using a combination of freeze-dried precursors and an anion-doping method. The results obtained using XRPD, SEM-EDS and the electrochemical measurements indicate the successful incorporation of the halogens into the $La_2CuO_{4-\delta}$ structure. The pellets of undoped $La_2CuO_{4-\delta}$ that sintered at 1000 °C showed Cu segregation on the surface; however, adequate halogen doping prevented this superficial segregation at high sintering temperatures. Moreover, the modification of the anionic network enhanced the bulk oxygen diffusion and surface oxygen exchange properties. The polarization resistance values for halogenated samples were lower than those for the pristine LCO, i.e., 0.20, 0.11 and 0.08 Ω cm^2 for LCO, $F_{0.1}$ and $Cl_{0.1}$, respectively, at 800 °C. These results indicate that halogen doping is an effective and promising strategy for improving the electrochemical performance of $La_2CuO_{4-\delta}$, as well as different electrode materials.

Supplementary Materials: The following supporting information can be downloaded at: https://www.mdpi.com/article/10.3390/pr10061206/s1, Figure S1. Impedance spectra of the Pt/LCO/CGO/LCO/Pt symmetrical cell (black solid line) and blank Pt/CGO/Pt (red solid line) at (a) 200 °C and (b) 600 °C.

Author Contributions: Conceptualization: L.d.S.-G. and D.M.-L.; methodology: L.d.S.-G., J.M.P.-V. and J.Z.-G.; investigation: L.d.S.-G. and J.Z.-G.; formal analysis: L.d.S.-G., J.M.P.-V., D.M.-L. and J.Z.-G.; validation: D.M.-L. and E.R.L.; visualization: L.d.S.-G. and D.M.-L.; project administration: D.M.-L.; writing—original draft: L.d.S.-G.; review and editing: J.M.P.-V., J.Z.-G., E.R.L. and D.M.-L. All authors have read and agreed to the published version of the manuscript.

Conflicts of Interest: The authors declare no conflict of interest.

References

1. Minh, N.Q. Ceramic Fuel Cells. *J. Am. Ceram. Soc.* **1993**, *76*, 563–588. [CrossRef]
2. Tahir, N.N.M.; Baharuddin, N.A.; Samat, A.A.; Osman, N.; Somalu, M.R. A review on cathode materials for conventional and proton-conducting solid oxide fuel cells. *J. Alloys Compd.* **2022**, *894*, 162458. [CrossRef]
3. Sabri, N.S.M.; Izman, S.; Kurniawan, D. Perovskite materials for intermediate temperature solid oxide fuel cells cathodes: A review. *AIP Conf. Proc.* **2020**, *2262*, 030013.
4. Gao, Z.; Mogni, L.V.; Miller, E.C.; Railsback, J.G.; Barnett, S.A. A perspective on low-temperature solid oxide fuel cells. *Energy Environ. Sci.* **2016**, *9*, 1602–1644. [CrossRef]
5. Bello, I.T.; Zhai, S.; He, Q.; Xu, Q.; Ni, M. Scientometric review of advancements in the development of high-performance cathode for low and intermediate temperature solid oxide fuel cells: Three decades in retrospect. *Int. J. Hydrog. Energy* **2021**, *46*, 26518–26536. [CrossRef]

6. Ahmad, M.Z.; Ahmad, H.S.; Chen, R.S.; Ismail, A.F.; Hazan, R.; Baharuddin, N.A. Review on recent advancement in cathode material for lower and intermediate temperature solid oxide fuel cells application. *Int. J. Hydrog. Energy* **2022**, *47*, 1103–1120. [CrossRef]

7. Paydar, S.; Shariat, M.H.; Javadpour, S. Investigation on electrical conductivity of LSM/YSZ8, LSM/$Ce_{0.84}Y_{0.16}O_{0.96}$ and LSM/$Ce_{0.42}Zr_{0.42}Y_{0.16}O_{0.96}$ composite cathodes of SOFCs. *Int. J. Hydrog. Energy* **2016**, *41*, 23145–23155. [CrossRef]

8. Chandran, P.R.; Arjunan, T. A review of materials used for solid oxide fuel cell. *Int. J. ChemTech Res.* **2015**, *7*, 488–497.

9. Zhang, L.; Chen, G.; Dai, R.; Lv, X.; Yang, D.; Geng, S. A review of the chemical compatibility between oxide electrodes and electrolytes in solid oxide fuel cells. *J. Power Sources* **2021**, *492*, 229630. [CrossRef]

10. Kumar, R.V.; Khandale, A.P. A review on recent progress and selection of cobalt-based cathode materials for low temperature-solid oxide fuel cells. *Renew. Sustain. Energy Rev.* **2022**, *156*, 111985. [CrossRef]

11. Li, Y.; Zhang, W.; Zheng, Y.; Chen, J.; Yu, B.; Chen, Y.; Liu, M. Controlling cation segregation in perovskite-based electrodes for high electro-catalytic activity and durability. *Chem. Soc. Rev.* **2017**, *46*, 6345–6378. [CrossRef] [PubMed]

12. Da Silva, F.S.; de Souza, T.M. Novel materials for solid oxide fuel cell technologies: A literature review. *Int. J. Hydrog. Energy* **2017**, *42*, 26020–26036. [CrossRef]

13. Majewski, A.J.; Khodimchuk, A.; Zakharov, D.; Porotnikova, N.; Ananyev, M.; Johnson, I.D.; Darr, J.A.; Slater, P.R.; Steinberger-Wilckens, R. Oxygen surface exchange properties and electrochemical activity of lanthanum nickelates. *J. Solid State Chem.* **2022**, *312*, 123228. [CrossRef]

14. Banner, J.; Akter, A.; Wang, R.; Pietras, J.; Sulekar, S.; Marina, O.A.; Gopalan, S. Rare earth Nickelate electrodes containing heavily doped ceria for reversible solid oxide fuel cells. *J. Power Sources* **2021**, *507*, 230248. [CrossRef]

15. Skinner, S.J.; Kilner, J.A. Oxygen diffusion and surface exchange in $La_{2-x}Sr_xNiO_{4+\delta}$. *Solid State Ion.* **2000**, *135*, 709–712. [CrossRef]

16. Baharuddin, N.A.; Muchtar, A.; Somalu, M.R. Short review on cobalt-free cathodes for solid oxide fuel cells. *Int. J. Hydrog. Energy* **2017**, *42*, 9149–9155. [CrossRef]

17. Ding, P.; Li, W.; Zhao, H.; Wu, C.; Zhao, L.; Dong, B.; Wang, S. Review on Ruddlesden–Popper perovskites as cathode for solid oxide fuel cells. *J. Phys. Mater.* **2021**, *4*, 022002. [CrossRef]

18. Benamira, M.; Ringuedé, A.; Cassir, M.; Horwat, D.; Lenormand, P.; Ansart, F.; Bassat, J.M.; Viricelle, J.P. Enhancing oxygen reduction reaction of YSZ/$La_2NiO_{4+\delta}$ using an ultrathin $La_2NiO_{4+\delta}$ interfacial layer. *J. Alloys Compd.* **2018**, *746*, 413–420. [CrossRef]

19. Tarutin, A.P.; Lyagaeva, J.G.; Medvedev, D.A.; Bi, L.; Yaremchenko, A.A. Recent advances in layered $Ln_2NiO_{4+\delta}$ nickelates: Fundamentals and prospects of their applications in protonic ceramic fuel and electrolysis cells. *J. Mater. Chem. A* **2021**, *9*, 154–195. [CrossRef]

20. Zinkevich, M.; Aldinger, F. Thermodynamic analysis of the ternary La–Ni–O system. *J. Alloys Compd.* **2004**, *375*, 147–161. [CrossRef]

21. Singh, K.; Ganguly, P.; Rao, C. Structural transitions in $(La, Ln)_2CuO_4$ and $La_2(Cu,Ni)O_4$ systems. *Mater. Res. Bull.* **1982**, *17*, 493–500. [CrossRef]

22. Li, Q.; Zhao, H.; Huo, L.; Sun, L.; Cheng, X.; Grenier, J.-C. Electrode properties of Sr doped La_2CuO_4 as new cathode material for intermediate-temperature SOFCs. *Electrochem. Commun.* **2007**, *9*, 1508–1512. [CrossRef]

23. Shijie, Z.; Na, L.; Liping, S.; Qiang, L.; Lihua, H.; Hui, Z. A novel high-entropy cathode with the A_2BO_4-type structure for solid oxide fuel cells. *J. Alloys Compd.* **2022**, *895*, 162548. [CrossRef]

24. Bo, L.; Na, L.; Liping, S.; Qiang, L.; Lihua, H.; Hui, Z. Rare-earth elements doped Nd_2CuO_4 as Cu-based cathode for intermediate-temperature solid oxide fuel cells. *J. Alloys Compd.* **2021**, *870*, 159397. [CrossRef]

25. Zhang, Z.; Du, Z.; Niemczyk, A.; Li, K.; Zhao, H.; Świerczek, K. A-site nonstoichiometry and B-site doping with selected M^{3+} cations in $La_{2-x}Cu_{1-y-z}Ni_yM_zO_{4-\delta}$ layered oxides. *Solid State Ion.* **2018**, *317*, 26–31. [CrossRef]

26. Goodenough, J.; Manthiram, A. Crystal chemistry and superconductivity in the copper oxides. In *Chemistry of High Temperature Superconductors*; World Scientific: Singapore, 1991; pp. 1–56.

27. Dos Santos-Gómez, L.; Porras-Vázquez, J.M.; Hurtado, J.; Losilla, E.R.; Marrero-López, D. Stability and electrochemical performance of nanostructured $La_2CuO_{4+\delta}$ cathodes. *J. Alloys Compd.* **2019**, *788*, 565–572. [CrossRef]

28. Huang, X.; Shin, T.H.; Zhou, J.; Irvine, J.T.S. Hierarchically nanoporous $La_{1.7}Ca_{0.3}CuO_{4-\delta}$ and $La_{1.7}Ca_{0.3}Ni_xCu_{1-x}O_{4-\delta}$ ($0.25 \leq x \leq 0.75$) as potential cathode materials for IT-SOFCs. *J. Mater. Chem. A* **2015**, *3*, 13468–13475. [CrossRef]

29. Kanai, H.; Mizusaki, J.; Tagawa, H.; Hoshiyama, S.; Hirano, K.; Fujita, K.; Tezuka, M.; Hashimoto, T. Defect chemistry of $La_{2-x}Sr_xCuO_{4-\delta}$: Oxygen nonstoichiometry and thermodynamic stability. *J. Solid State Chem.* **1997**, *131*, 150–159. [CrossRef]

30. Mazo, G.; Savvin, S. The molecular dynamics study of oxygen mobility in $La_{2-x}Sr_xCuO_{4-\delta}$. *Solid State Ion.* **2004**, *175*, 371–374. [CrossRef]

31. Zhang, L.; Sun, W.; Xu, C.; Ren, R.; Yang, X.; Qiao, J.; Wang, Z.; Sun, K. Attenuating a metal–oxygen bond of a double perovskite oxide via anion doping to enhance its catalytic activity for the oxygen reduction reaction. *J. Mater. Chem. A* **2020**, *8*, 14091–14098. [CrossRef]

32. Zhang, Z.; Zhu, Y.; Zhong, Y.; Zhou, W.; Shao, Z. Anion Doping: A New Strategy for Developing High-Performance Perovskite-Type Cathode Materials of Solid Oxide Fuel Cells. *Adv. Energy Mater.* **2017**, *7*, 1700242. [CrossRef]

33. Zhang, Y.; Zhu, Z.; Gu, Y.; Chen, H.; Zheng, Y.; Ge, L. Effect of Cl doping on the electrochemical performance of $Sr_2Fe_{1.5}Mo_{0.5}O_{6-\delta}$ cathode material for solid oxide fuel cells. *Ceram. Int.* **2020**, *46*, 22787–22796. [CrossRef]

34. Hou, N.; Gan, J.; Yan, Q.; Zhao, Y.; Li, Y. Improved electrochemical oxidation kinetics of $La_{0.5}Ba_{0.5}FeO_{3-\delta}$ anode for solid oxide fuel cells with fluorine doping. *J. Power Sources* **2022**, *521*, 230932.

35. Guan, R.; Wang, Z.; Xu, H.; Hao, X.; Yang, L.; Liu, J.; Yu, S.; He, T. Manipulating the Activity and Thermal Compatibility of $NdBaCoFeO_{5+\delta}$ Cathodes for Intermediate-Temperature Solid Oxide Fuel Cells via Fluorine Doping. *ACS Appl. Energy Mater.* **2022**, *5*, 481–491. [CrossRef]

36. Wang, W.; Zhang, X.; Zhang, D.; Zeng, Q.; Jiang, Y.; Lin, B. Highly promoted performance of triple-conducting cathode for YSZ-based SOFC via fluorine anion doping. *Ceram. Int.* **2020**, *46*, 23964–23971. [CrossRef]

37. Li, G.; Gou, Y.; Ren, R.; Xu, C.; Qiao, J.; Sun, W.; Wang, Z.; Sun, K. Fluorinated $Pr_2NiO_{4+\delta}$ as high-performance air electrode for tubular reversible protonic ceramic cells. *J. Power Sources* **2021**, *508*, 230343. [CrossRef]

38. Adachi, S.; Wu, X.J.; Tamura, T.; Tatsuki, T.; Tokiwa-Yamamoto, A.; Tanabe, K. Synthesis and superconducting properties of fluorinated La_2CuO_4 using NH_4F. *Phys. C Supercond.* **1997**, *291*, 59–66. [CrossRef]

39. Tressaud, A.; Robin, C.; Chevalier, B.; Lozano, L.; Etourneau, J. Superconductivity in chlorine-treated La_2CuO_4. *Phys. C Supercond.* **1991**, *177*, 330–336. [CrossRef]

40. Mi, S.; Liu, Z.; Luo, C.; Cai, L.; Zhang, Z.; Li, L. A review on preparing new energy ultrafine powder materials by freeze-drying. *Dry. Technol.* **2020**, *38*, 1544–1564. [CrossRef]

41. Zakaria, Z.; Awang Mat, Z.; Hassan, S.H.A.; Kar, Y.B. A review of solid oxide fuel cell component fabrication methods toward lowering temperature. *Int. J. Energy Res.* **2020**, *44*, 594–611. [CrossRef]

42. Zamudio-García, J.; Porras-Vázquez, J.M.; dos Santos-Gómez, L.; Losilla, E.R.; Marrero-López, D. Effect of Zn addition on the structure and electrochemical properties of co-doped $BaCe_{0.6}Zr_{0.2}Ln_{0.2}O_{3-\delta}$ (Ln = Y, Gd, Yb) proton conductors. *Ceram. Int.* **2018**, *44*, 14113–14121. [CrossRef]

43. Amelo, B. *Pert HighScore Plus, Version 3.0 e.*; Malvern Panalytical: Almelo, The Netherlands, 2012.

44. Larson, A.; Von Dreele, R. Los Alamos National Laboratory Report No. LA-UR-86-748. 1994. Available online: https://11bm.xray.aps.anl.gov/documents/GSASManual.pdf (accessed on 12 May 2022).

45. Zhang, Y.; Shen, L.; Wang, Y.; Du, Z.; Zhang, B.; Ciucci, F.; Zhao, H. Enhanced oxygen reduction kinetics of IT-SOFC cathode with $PrBaCo_2O_{5+\delta}/Gd_{0.1}Ce_{1.9}O_{2-\delta}$ coherent interface. *J. Mater. Chem. A* **2022**, *10*, 3495–3505. [CrossRef]

46. Dos Santos-Gómez, L.; Porras-Vázquez, J.M.; Losilla, E.R.; Marrero-López, D. Improving the efficiency of layered perovskite cathodes by microstructural optimization. *J. Mater. Chem. A* **2017**, *5*, 7896–7904. [CrossRef]

47. Wan, T.H.; Saccoccio, M.; Chen, C.; Ciucci, F. Influence of the Discretization Methods on the Distribution of Relaxation Times Deconvolution: Implementing Radial Basis Functions with DRTtools. *Electrochim. Acta* **2015**, *184*, 483–499. [CrossRef]

48. *Inorganic Crystal Structure Database (ICSD), v2018-01. General Structure Analysis System*; FIZ Karlsruhe GmbH: Karlsruhe, Germany, 2018.

49. Singh, R.P.; Arora, P.; Nellaiappan, S.; Shivakumara, C.; Irusta, S.; Paliwal, M.; Sharma, S. Electrochemical insights into layered La_2CuO_4 perovskite: Active ionic copper for selective CO_2 electroreduction at low overpotential. *Electrochim. Acta* **2019**, *326*, 134952. [CrossRef]

50. Zheng, K.; Gorzkowska-Sobas, A.; Swierczek, K. Evaluation of Ln_2CuO_4 (Ln: La, Pr, Nd) oxides as cathode materials for IT-SOFCs. *Mater. Res. Bull.* **2012**, *47*, 4089–4095. [CrossRef]

51. Chevalier, B.; Tressaud, A.; Brisson, C.; Dance, J.M.; Etourneau, J.; Tuilier, M.H.; Soubeyroux, J.L.; Cassart, M.; Issi, J.P. Anionic Intercalation in La_2CuO_4 Oxide by Fluorine or Chlorine Treatment. *Mol. Cryst. Liq. Cryst. Sci. Technol. Sect. A Mol. Cryst. Liq. Cryst.* **1994**, *244*, 135–142. [CrossRef]

52. Osinkin, D.A. An approach to the analysis of the impedance spectra of solid oxide fuel cell using the DRT technique. *Electrochim. Acta.* **2021**, *372*, 137858. [CrossRef]

53. Xia, J.; Wang, C.; Wang, X.; Bi, L.; Zhang, Y. A perspective on DRT applications for the analysis of solid oxide cell electrodes. *Electrochim. Acta* **2020**, *349*, 136328.

54. Osinkin, D.A. Detailed analysis of electrochemical behavior of high–performance solid oxide fuel cell using DRT technique. *J. Power Sources* **2022**, *527*, 231120. [CrossRef]

55. Lee, J.G.; Park, M.G.; Yoon, H.H.; Shul, Y.G. Application of GDC-YDB bilayer and LSM-YDB cathode for intermediate temperature solid oxide fuel cells. *J. Electroceramics* **2013**, *31*, 231–237. [CrossRef]

56. Takeda, Y.; Kanno, R.; Noda, M.; Tomida, Y.; Yamamoto, O. Cathodic polarization phenomena of perovskite oxide electrodes with stabilized zirconia. *J. Electrochem. Soc.* **1987**, *134*, 2656–2661. [CrossRef]

57. Jiang, Z.; Lei, Z.; Ding, B.; Xia, C.; Zhao, F.; Chen, F. Electrochemical characteristics of solid oxide fuel cell cathodes prepared by infiltrating $(La,Sr)MnO_3$ nanoparticles into yttria-stabilized bismuth oxide backbones. *Int. J. Hydrog. Energy* **2010**, *35*, 8322–8330. [CrossRef]

58. Almar, L.; Szász, J.; Weber, A.; Ivers-Tiffée, E. Oxygen Transport Kinetics of Mixed Ionic-Electronic Conductors by Coupling Focused Ion Beam Tomography and Electrochemical Impedance Spectroscopy. *J. Electrochem. Soc.* **2017**, *164*, F289–F297.

59. Marrero-López, D.; Romero, R.; Martín, F.; Ramos-Barrado, J.R. Effect of the deposition temperature on the electrochemical properties of $La_{0.6}Sr_{0.4}Co_{0.8}Fe_{0.2}O_{3-\delta}$ cathode prepared by conventional spray-pyrolysis. *J. Power Sources* **2014**, *255*, 308–317. [CrossRef]